

Cite this: *J. Mater. Chem. C*, 2017,
5, 11275

Langmuir films and uniform, large area, transparent coatings of chemically exfoliated MoS₂ single layers†

Yefeng Zhang,^a Luzhu Xu,^a Wesley R. Walker,^a Collin M. Tittle,^b
Christopher J. Backhouse^b and Michael A. Pope^{id}*^a

By manipulating colloidal dispersions of chemically exfoliated molybdenum disulfide (MoS₂) into an appropriate spreading solvent, we demonstrate, for the first time, the ability to form stable, floating MoS₂ Langmuir films without the use of surfactants or significant material loss into the aqueous sub-phase. While the floating sheets can be compressed into a densely tiled film by the barriers of a traditional Langmuir–Blodgett trough, we also report an edge-to-edge aggregation and spreading driven densification phenomena that allows the film to be built up from the outside of the trough inwards during the deposition process. Continued deposition allows us to fill the entire trough with a dense (85–95% coverage) film of discretely tiled 1T MoS₂ nanosheets and to coat substrates as large as 130 cm². The transfer efficiency is found to be as high as 120 m² of coated area per gram of deposited MoS₂. Comparing the transfer efficiency to the theoretical specific surface area of MoS₂ provides a method to estimate film thickness and exfoliation efficiency. Atomic force microscopy and optical absorption measurements are used to corroborate this estimate of 2.7 layers for the traditional *n*-butyllithium exfoliation method used. We demonstrate that the films can be built up layer-by-layer and investigate the optical and electrical properties of the films before and after conversion from the 1T to 2H polymorph.

Received 13th June 2017,
Accepted 17th July 2017

DOI: 10.1039/c7tc02637d

rsc.li/materials-c

Introduction

Molybdenum disulfide (MoS₂) is a transition metal dichalcogenide (TMD) that has attracted significant attention due to its special electronic, optical, and chemical properties.^{1–6} MoS₂ and other 2D metal dichalcogenides can exist in various polymorphs. Bulk MoS₂ is typically found in the 2H polymorph which is a semiconductor possessing an indirect bandgap of ~1.2 eV.⁷ This can be converted from the 2H to the 1T polymorph, a metallic phase, through chemical exfoliation.⁸ However, this 1T polymorph is metastable and can be converted back to the 2H polymorph by thermal annealing at ~150–450 °C.^{4,9} A layer number dependency has been observed in both the optical and electrical properties of MoS₂.⁴ With a decreasing layer number, an increase in the bandgap to 1.9 eV as well as a transition from an indirect to direct bandgap has been observed.⁴ These properties have established MoS₂ as a promising material

for future applications in electronic and photonic devices such as transparent semiconductors,^{10,11} solar cells,^{6,12} supercapacitors^{5,13,14} and sensors.¹⁵ Furthermore, metallic MoS₂ has demonstrated significant promise as an efficient electrocatalyst for the hydrogen evolution reaction (HER)^{16–19} as well as in photoelectrochemical (PEC) water splitting.^{3,20,21}

Significant research has been carried out to discover and improve synthesis methods of MoS₂ nanosheets by chemical and solution exfoliation of bulk precursors.^{5,22,23} However, there has been comparatively less development of well-controlled film deposition techniques. While physical and chemical vapor deposition (CVD) yield fine control over film properties, the high temperatures, high vacuum conditions and required transfer steps currently hinder scale-up.^{6,24} On the other hand, traditional methods such as vacuum filtration offer a fast and cost-effective way to prepare thin films.⁵ However, these methods are either limited to small area coatings or lack nanometer-scale control of the film thickness. Recently, a more advanced film forming process was developed for depositing WSe₂, another member of the TMD family, by assembling the material at the ethylene glycol–hexane liquid–liquid interface.²⁵ Since both ethylene glycol and hexane are non-solvents for WSe₂, the liquid–liquid interface offers a strong spatial confinement for WSe₂ flakes, reducing the possibility of aggregation and overlapping.²⁵

^a Quantum-Nano Centre, Department of Chemical Engineering,
University of Waterloo, Waterloo N2L 3G1, Canada.
E-mail: michael.pope@uwaterloo.ca

^b Quantum-Nano Centre, Department of Electrical Engineering,
University of Waterloo, Waterloo N2L 3G1, Canada

† Electronic supplementary information (ESI) available. See DOI: 10.1039/c7tc02637d

A similar and earlier approach for MoS₂ was reported where the MoS₂ was confined at the water–1-hexene interface by shaking the two immiscible liquids.²⁶ These reports both demonstrated thin films with excellent overall uniformity. However, transfer of the films to a substrate is challenging.

In contrast to all abovementioned methods, the preparation of Langmuir films at the air–water interface, their densification through compression, and film transfer to substrates by the Langmuir–Blodgett (LB) deposition technique, is recognized as a facile and powerful approach to controllably fabricate molecular monolayer thin films on a variety of substrates.²⁷ This method was originally used to prepare ordered thin films of amphiphilic molecules such as lipids or surfactants,^{14,15} but has recently been extended to prepare thin films of various other nanomaterials such as gold and silver nanoparticles,^{28,29} single-walled carbon nanotubes,^{30–32} and graphene oxide.^{33–37} Notably, in 2008, Cote *et al.*³⁶ reported the first successful attempt of using the LB assembly technique to fabricate floating monolayers of graphene oxide (GO). They demonstrated that the density or surface coverage of the floating, repulsive GO sheets could be tuned by compressing the floating film using the moveable barriers of a commercial LB trough. Around the same time, Li *et al.*³⁸ reported the successful LB transfer of graphene sheets from the air–water interface. With multiple depositions, they were able to prepare a three-layer film with a sheet resistance of 8 k Ω and transparency over 80%. While, in principle, this method could also be applied to exfoliated MoS₂, so far, there have been no reported attempts to directly assemble MoS₂ at the air–water interface. This is likely because exfoliated MoS₂ sheets form stable dispersions mainly in water or water-miscible solvents (*e.g.* DMF, NMP, isopropanol, *etc.*). However, ideally a water-immiscible solvent should be used to avoid mixing between the spreading solvent and the sub-phase water to limit material loss within and contamination of the sub-phase water. To facilitate transfer of MoS₂ to the air–water interface, researchers have used charged, amphiphilic molecules to coordinate with the negatively charged MoS₂.³⁹ Specifically, dihexadecyldimethylammonium bromide (DHA⁺Br[−]) was spread on the surface of a chemically exfoliated MoS₂/H₂O suspension to create a uniform monolayer of DHA⁺Br[−]. Due to the electrostatic interaction between positively charged DHA⁺ and the negatively charged MoS₂, a hybrid DHA⁺/MoS₂ film was formed and could be transferred to substrates by LB deposition. While theoretically, a densely-packed MoS₂ thin film can then be achieved by further removing the cationic amphiphilic components, practically, it is challenging to do so without either disturbing the film or leaving residue.

To overcome these challenges, in this work, we report a mixed-solvent colloidal dispersion strategy that allows us to transfer nearly 100% of chemically exfoliated 1T MoS₂ to the air–water interface without the assistance of any surfactants. When a high concentration spreading dispersion is used, we observe that MoS₂ sheets spontaneously aggregate into densely tiled islands near the LB trough edge. We hypothesize that this directed film assembly is correlated with the spreading pressure exerted by the spreading solvent during the dripping process

(*i.e.* spreading-assisted assembly). Using this approach, we demonstrate the assembly of large area MoS₂ thin films which cover the entire trough surface without the use of any adjustable barriers to densify the films. Compression with barriers is a requirement of the typical LB approach that limits film area and precludes continuous material deposition and transfer. Using our barrier-free method, we estimate transfer efficiencies as high as 120 m² of covered area per gram of deposited MoS₂. This allows us to calculate an average layer number of ~ 2.7 using the theoretical specific surface area of MoS₂ as calculated from crystal lattice parameters. This estimate is confirmed by analysis of height distribution data extracted from AFM images as well as by analyzing the optical absorption of the resulting film. This agreement suggests that we achieve nearly 100% transfer efficiency. While the average film thickness is 2.7 layers, the film is composed of 40–50% single layers, 10–15% double layers and 10–15% triple layers with a small population of thicker sheets which varies slightly from sample to sample. We study the film formation process as a function of time to elucidate the dynamics involved in film growth by video microscopy. We also demonstrate that this process can be carried out with simple and inexpensive equipment (*i.e.*, a Teflon coated glass dish). The directionality of the 2D aggregation process lends itself to the possibility of continuous film deposition and transfer, which has the potential to provide a simple and versatile path towards coatings for advanced electronic and optoelectronic applications.

Experimental methods

Chemical exfoliation and annealing

The chemical exfoliation method was adapted from ref. 4. Briefly, 0.5 g of MoS₂ powder (Sigma Aldrich, $\sim 6 \mu\text{m}$) was mixed with 7 mL of 1.6 M *n*-butyllithium solution in hexane (Sigma Aldrich) in a 25 mL flask filled with nitrogen gas for three days. The intercalated MoS₂ was washed with 80 mL of hexane, collected by filtration through Whatman[™] 42 filter paper and then transferred to a large beaker in a glove bag filled with nitrogen gas. 150 mL of DI water was added to the beaker immediately after the transfer. The beaker was then bath ultrasonicated (TruSonik, 2.5 L, 120 W) for 1 h to aid in exfoliating the material. During the sonication process, ice was added to the bath water every 20 min to avoid overheating the solution. XRD analysis of MoS₂ powder before and after chemical exfoliation were obtained in a PANalytical Empyrean diffractometer using Cu K α radiation. Zeta potential was measured in various pH buffers using a Malvern Zetasizer Nano ZS90 instrument with freshly prepared MoS₂ aqueous dispersion. The MoS₂ aqueous dispersion was prepared by washing the MoS₂ dispersion obtained from chemical exfoliation with deionized water. Citrate buffer was used for pH = 3 with an ionic strength of 100 mM. HEPES (4-(2-hydroxyethyl)-1-piperazineethanesulfonic acid) buffer was used for pH = 7.6 with an ionic strength of 10 mM and phosphate buffer was used for pH = 6, 7, 8 with an ionic strength of 100 mM.

Solvent exchange

After bath sonication, 80 mL of the dispersion was transferred to two beakers and 0.48 mL of 10% HCl solution was added to each to adjust the pH of the dispersion to 2. The dispersion was then left undisturbed for 12 h at room temperature. Afterwards, the top two thirds of the solvent in each beaker was removed by pipetting and the aggregates of MoS₂ at the bottom of both beakers were collected by filtration using Whatman 42 filter paper and washed with 5 mL of water followed by 5 mL of dimethylformamide (DMF). The filter cake was not allowed to dry completely to avoid the formation of aggregates that could not be redispersed (*i.e.*, hard aggregates). The filter cake was transferred to a centrifuge tube and 40 mL of DMF was then added to the tube. The aggregate was redispersed by bath-sonication for 30 min and then centrifuged at 2000 rpm for 15 min using a Thermo Scientific Centra CL2 centrifuge. The top 35 mL of the dispersion was collected for future use. The MoS₂ concentration of the as-prepared MoS₂/DMF dispersion was determined by measuring the mass difference before and after evaporating 5 mL of the dispersion in a glass vial using a vacuum oven. The final spreading dispersion was prepared by mixing the as-made MoS₂/DMF dispersion with residue-free 1,2-dichloroethane (DCE) (Fisher Scientific, 99%) at a 1:1 volume ratio. The MoS₂/DCE dispersion was prepared similarly, except using DCE as the solvent to disperse MoS₂.

Langmuir–Blodgett trough analysis

The surface pressure–area (π - A) isotherm was measured using a KSV Minitrough (System 2). The polytetrafluoroethylene (PTFE) trough was cleaned by wiping with chloroform and rinsing with deionized (DI) water. Approximately 180 mL of deionized water ($\sim 18\text{ M}\Omega$) was added to the trough and the cleanliness of the water surface was examined by monitoring the change in surface pressure while the barriers of the trough were being closed. The surface was cleaned by a vacuum aspirator until the surface pressure changed by less than 0.02 mN m^{-1} after compression. In a typical spreading process, the MoS₂/DMF/DCE dispersion was dripped onto the water surface ($\sim 250\text{ cm}^2$) at a flow rate of 0.1 mL min^{-1} controlled by a syringe pump (KD Scientific) using PTFE tubing with 0.312 mm outer diameter. The distance between the tip of the tubing and the water surface was made as close as possible without the drop touching the air–water interface to prevent the liquid drop (which is denser than water) from penetrating through the interface and into the water. The spreading process was stopped when about half of the water surface was covered by MoS₂ as could be observed visually as a faint dark film. The compression of the film was carried out at a barrier speed of 15 mm min^{-1} until the surface pressure reached $\sim 14\text{ mN m}^{-1}$. The expansion process was carried out at the same speed immediately after the compression.

Spreading-assisted film densification

For most experiments, a custom glass trough with PTFE-coated walls and a PTFE-coated barrier were extensively washed with DI water to remove any possible water-soluble contaminants

and wiped with DCE to remove any possible organic contaminants. The trough was then filled with deionized water. The glass syringe was washed with DI water first and then with DCE for the same purpose. For the spreading, the same syringe, tubing, pump and flow rate were applied as in the LB assembly. The total available water surface area ($15.8\text{ cm} \times 12.7\text{ cm}$) for the spreading is $\sim 200\text{ cm}^2$. The film was deposited by dripping the dispersion through a PTFE tube with inner and outer diameter of 0.159 and 0.312 mm, respectively. The flow rate was set to 0.1 mL min^{-1} via the syringe pump. The deposition of the film was carried out using the horizontal precipitation method: freshly cleaved mica or clean glass slides to be coated were placed in the trough below the level of the water sub-phase (before cleaning the air–water interface) and the film was slowly lowered onto the substrate by withdrawing water from the trough.⁴⁰ To convert the as-deposited MoS₂ films to the semiconducting 2H polymorph, the samples were annealed in a tube furnace at $150\text{ }^\circ\text{C}$ for 1 h under Ar gas by evacuating and filling the tube with ultrahigh purity Ar (99.999%) three times.

Film characterization

The UV-Vis absorption spectra of MoS₂/DMF dispersions were taken using an Agilent 8453 instrument. The transmittance measurements of deposited films on glass substrate were carried out using the same instrument. AFM images were taken using a Digital Instruments Nanoscope IV in contact mode using silicon nitride tips (Bruker, NP-STT10). The fractional coverage and average sheet thickness of the deposited MoS₂ film was determined by analyzing AFM images of these films using a custom Python script. Briefly, the AFM image was divided into quadrants (to reduce variations in the substrate height over the large $10 \times 10\text{ }\mu\text{m}$ scan area), then the sum of 20 Gaussian curves was fit to the raw height data of each quadrant before combining all four outputs. The initial guesses for the curve parameters were determined by manually measuring the step height at substrate–monolayer and monolayer–bilayer junctions. The fractional coverage was defined as the area under each curve in their respective bin. Absorption measurements for the Tauc analysis and optical thickness estimates were taken with a Shimadzu UV-1601PC UV-Vis double-beam spectrometer and the absorption was measured from 900 to 300 nm. A 150 W Xenon light source with a 10 nm beam width monochromator was used to provide excitation light. Raman spectra were collected using a Horiba HR800 spectrometer operating at $\lambda = 532\text{ nm}$.

A standard challenge in electrical characterization is to contact samples without damaging or substantially changing their characteristics. In clean room fabrication, electrodes are often lithographically deposited onto samples. However, such an approach is not conducive to rapid prototyping. To contact MoS₂ samples on glass substrates, a fabrication procedure for conformal electrodes made from a heterostructure of carbon tape and indium tin oxide (ITO) coated plastic was developed. This allowed for electrodes to be adhered to previously prepared samples without damaging the fragile monolayers or

substantially changing their electrical properties. The carbon tape/ITO interdigitated electrode structures were fabricated using ITO-coated polyethylene terephthalate (PET, Adafrit, 1309), 8 mm wide carbon tape (Ted Pella, 16073), copper tape with a conductive adhesive (Ted Pella, 16072-1), and 22 AWG copper wires. The carbon tape is adhered to the ITO side of a small section of PET. The pattern, designed in Asymptote was cut through the carbon tape and ITO, leaving just the PET support intact, using an IR laser (Universal Laser Systems VLS 2.30 CO₂ laser 10.6 μm) at 8% power, 10% speed, 1000 ppi and a focus of 0.1 mm. The design left a 100 μm gap over a length of 408 mm between the two electrode contacts. As the ITO has a very low resistance, the main source of resistance in this configuration is the vertical resistance through the carbon tape. Thus, the effective series resistance is comprised of the vertical resistance through the carbon tape combined with the transverse resistance through the ITO to the contacts on the exterior. Each end of the structure is contacted by the adhesive copper tape which has negligible resistance relative to the rest of the structure. Wire leads are soldered onto the copper tape for reproducible contact with alligator clips. The effective resistance of the electrode structure was measured by adhering a sheet of ITO to an electrode structure. An Agilent 1252A Digital

Multimeter was used to measure the resistance of the various samples. The system was validated by measuring the conductivity of ITO.

Results and discussion

Mixed-solvent colloidal dispersion

To efficiently transfer the exfoliated MoS₂ to the air–water interface, a water-immiscible and volatile spreading solvent such as chloroform or DCE is preferred.⁴¹ However, the MoS₂ nanosheets obtained from the chemical exfoliation method are well dispersed in water. Thus, our first goal was to engineer a non-aqueous colloidal dispersion to facilitate efficient transfer of material to the air–water interface. As described schematically in Fig. 1, we carried this out through a reversible aggregation and solvent exchange method. MoS₂ was chemically exfoliated by first lithiating MoS₂ with *n*-butyllithium, followed by exfoliation of this reactive material by mixing with water.^{4,5} It is known that this causes the decomposition of water and the build-up of H₂ gas between adjacent sheets of MoS₂ which results in their exfoliation.^{23,42} The resulting dark coloured and colloiddally stable dispersion in water is shown in Fig. 1a. The addition

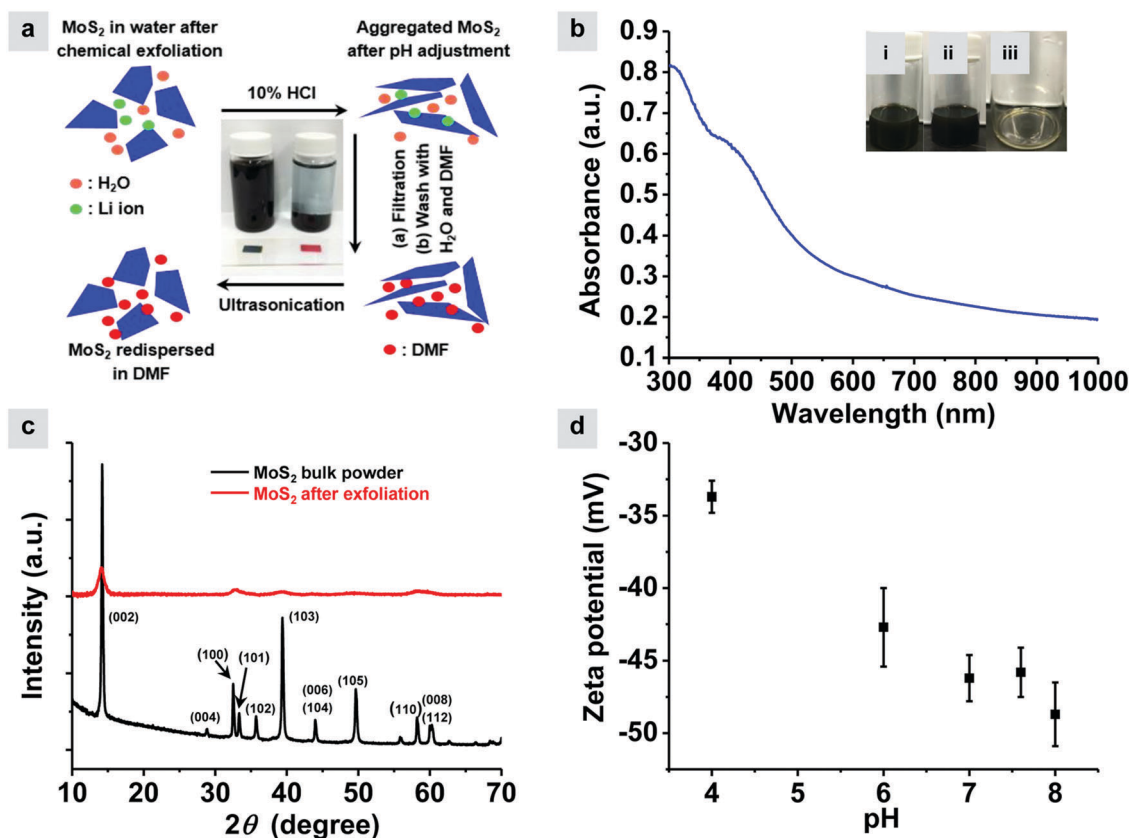


Fig. 1 (a) Solvent exchange method. Middle picture: adjusting the pH to ~2 causes the aggregation of MoS₂. (b) UV-Vis absorption spectra of the MoS₂/DMF dispersion after solvent exchange. The inset shows the stability analysis of the MoS₂/DMF/DCE dispersion: (i) the freshly prepared dispersion; (ii) the dispersion after one week; (iii) the bottom of the vial after slowly removing the dispersion – no precipitate was found at the bottom of the vial for the dispersion after 1 week. (c) XRD profiles of MoS₂ powders before (black line) and after (red line) chemical exfoliation, HCl – induced flocculation and drying. (d) Plot of zeta potential as a function of pH for the MoS₂ dispersion in water.

of HCl to this dispersion caused the MoS₂ to flocculate. Previous studies have shown that chemically exfoliated MoS₂ will precipitate in HCl solution at a pH \sim 2.⁴³ While the mechanism of this aggregation behaviour has not been explored, it is likely due to the shielding of the electrostatic double layer force between MoS₂ which are known to be negatively charged after being reduced by *n*-butyllithium to produce the salt Li⁺MoS₂⁻.⁴⁴ To confirm the charge on the MoS₂ nanosheets, the zeta potential in water was estimated to be between about -39 mV to -49 mV over a pH range of 4–8, assuming that the flat plates behave hydrodynamically as spherical particles. This is congruent with several other reports which have measured a zeta potential of -43 mV, presumably, at near neutral pH.^{9,45} As a result of the charge screening by dissolved HCl, the attractive van der Waals forces between MoS₂ nanosheets overcomes their electrostatic repulsion, leading to their flocculation. After 12 h, the aggregated MoS₂ sediments to the bottom of the vial (Fig. 1a).

The precipitates were collected by filtration and could be redispersed in non-aqueous solvents by low power bath ultrasonication. The fact that the precipitates could be redispersed may be explained by considering that the sheets remained solvated in the aggregate, which provides steric hindrance against irreversible aggregation. To show the versatility of our solvent exchange method, we prepared both the MoS₂/DMF dispersion and MoS₂/DCE dispersion in preliminary trials. To confirm the successful exfoliation of MoS₂ by our procedure, we conducted UV-Vis measurements on the as-prepared MoS₂/DMF dispersion. It is known that the MoS₂ will undergo a transition from the 2H polymorph to the 1T polymorph during the chemical exfoliation process. The resulting 1T MoS₂ is metallic and thus no absorbance peaks should be observed at \sim 610 nm and \sim 660 nm which correspond to the A1 and B1 direct excitonic transitions in 2H MoS₂.⁴ This is confirmed by the absorbance spectra of the dispersion (Fig. 2b) where no discernable peaks are observed between 600 nm and 700 nm, which indicates that our chemical exfoliation is effective. Furthermore, XRD carried out after drying the washed precipitate indicates that the (00*l*) reflections, such as (002), (004) and (006), are significantly broadened and reduced in intensity. This confirms that our chemical exfoliation and centrifugation approach eliminated most large MoS₂ crystallites. A detailed analysis of the width of the (002) peak indicates that, after drying, the partially restacked powder has a fraction of crystallites which are approximately 10 layers thick.⁴⁶

For spreading, DCE is an ideal solvent since it is water-immiscible, spontaneously spreads at the air–water interface, and is volatile. However, we found that MoS₂ was poorly dispersed in DCE after solvent exchange and the resulting MoS₂/DCE dispersion was unstable. On the other hand, we observe that the MoS₂/DMF dispersion is stable over long periods of time but DMF is non-volatile and completely miscible with water. Since both DMF and DCE are miscible, we also tried mixtures of the two solvents to disperse MoS₂. We hypothesized that in this mixed-solvent colloidal system, the DMF would help stabilize the MoS₂ nanosheets and the DCE would help reduce the mixing of solvent and sub-phase water during repetitive dripping.

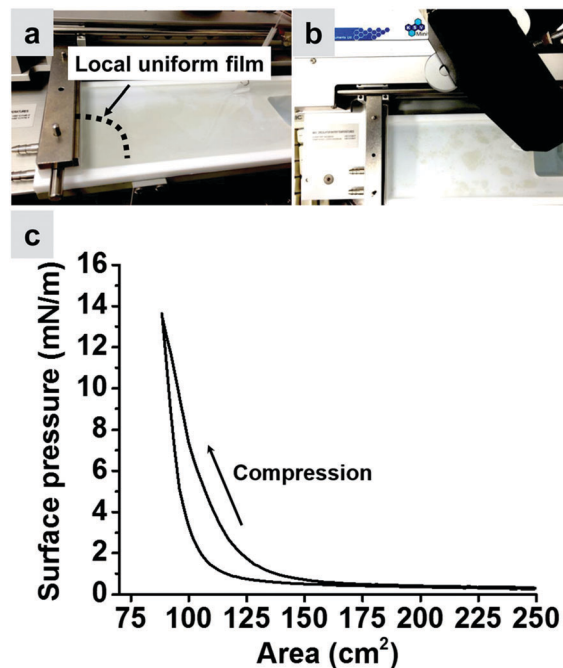


Fig. 2 The LB assembly of MoS₂ nanosheets using the mixed solvent DMF/DCE dispersion. (a) MoS₂ nanosheets floating on the water surface. (b) The aggregated MoS₂ nanosheets after expansion. (c) The compression–expansion isotherm.

As shown in Fig. 1c, to test our hypothesis, we first studied the stability of the MoS₂/DMF/DCE dispersion with a ratio of DMF to DCE of 1 : 1 (vol/vol). As illustrated in Fig. 1(b), the dispersion was found to remain stable even after one week, with no detectable sediment at the bottom of the vial.

Traditional Langmuir–Blodgett approach

To illustrate the importance of DCE in terms of transfer efficiency during the deposition, we conducted two experiments using a commercial LB trough. First, we tried to directly spread the MoS₂/DMF dispersion at the air–water interface. We observed that most drops entered the water sub-phase during the spreading process. Very few MoS₂ nanosheets were found floating on the water surface after a large volume of the dispersion was added. This observation indicated a strong mixing process occurred during the spreading since DMF is a water-miscible solvent. Next, we tested our mixed solvent (DMF/DCE) dispersion. After only a small volume was added, MoS₂ could be observed as a yellowish brown film by the naked eye. More careful observation found that MoS₂ nanosheets near the trough edge were aggregated into small islands. As more and more material was added to the air–water interface, these small islands were observed to form larger islands which eventually grew to a locally uniform film (*i.e.* in terms of its color) as shown in Fig. 2a. Once the film covered nearly 50% of the trough surface, the moveable barriers of the LB trough were used to collect surface pressure–area (π -*A*) isotherms. The surface pressure is defined as $\pi = \gamma_{\text{water}} - \gamma$ where γ_{water} is the surface tension of pure water (confirmed to be 72 mN m⁻¹ before the start of the experiment) and γ is the

measured surface tension during compression. The π - A isotherm is shown in Fig. 2c. Initially, π is nearly constant from 250 cm² to 150 cm² with a slight increase from zero due to the reduction in surface tension caused by the dissolution of DMF in the sub-phase water. At about 150 cm², π increased significantly and corresponds to the point where the islands begin to coalesce. At 14 mN m⁻¹, a dense film covered the entire trough. Expansion was carried out immediately after compression to 14 mN m⁻¹. The π - A isotherm upon expansion decreased more rapidly as the larger islands that formed upon compression broke into smaller fragments as shown in Fig. 2b.

The dispersion concentration was reduced to determine its impact on the observed 2D aggregates. It was found that the islands shrunk in size when a more dilute dispersion was spread at the air-water interface. However, this required us to add a significant volume of dispersion to the trough and larger islands eventually grew. Unfortunately, due to limitations in the expansion ratio of the trough used, defined as the total expanded trough area to the smallest compressed area ~ 3 , it was not possible to compress a dilute film to a density where a measurable pressure increase could be observed. Therefore, it was not possible to use the LB trough in the typical way; traditionally when small molecules such as lipids are added to the trough, the concentration of the spreading solution is often quite high (10–100 mg mL⁻¹) and only one drop of material or injection from a syringe is required to generate a film in the gas phase. The gas phase is compressed until it transitions to liquid, liquid-condensed and solid phases. The resulting uniform films can be compressed and expanded reversibly so that they can be deposited repetitively on substrates by dip coating *via* the traditional Langmuir-Blodgett process.^{34,36} The formation of aggregates, in our case, precludes such a process as the islands do not coalesce uniformly over the trough area during barrier compression. This aggregation phenomenon is surprising considering the relatively high zeta potential of MoS₂ measured in water (> -40 mV). For example, it has been suggested that graphene oxide, with a similar zeta potential, acts as repulsive objects when floating on water. However, others have shown that attractive van der Waals forces and other long-range attractive forces can dominate under certain conditions.⁴⁷ The graphene oxide case is also complicated by the fact that much of the material is lost into the sub-phase; G. J. Silverberg *et al.* report up to 99% loss.⁴⁷

Spreading-assisted film densification

Instead of stopping the process of material transfer to the air-water interface and using the trough barriers to compress the film, we carried out an experiment where dripping was continued. Since barriers of a commercial LB trough were not required for this experiment, we simply used a clean glass water bath with Teflon tape to make the edges hydrophobic and a Teflon tape wrapped fixed barrier. Fig. 3 shows the evolution of the film as more MoS₂ dispersion is added at the air-water interface. The islands grow from the trough edges and eventually spanned the entire width of the trough growing towards the center. The dripping was stopped when the available area

for spreading the dispersion was so small that the solvent began to pool and the next drop no longer spread, forming a solvent lens at the injection point. At this point, the entire trough area was covered with a film of uniform tint. The as-formed MoS₂ film was stable at the air-water interface, as shown in Fig. 3c, where a clear film boundary remained for hours after the fixed barrier was removed suggesting that the floating film had reached the solid phase and was clearly not repulsive.

The film growth phenomenon was further examined by analyzing video taken during the deposition process. (see Videos in ESI†) Upon spreading of the first drop of dispersion, isolated aggregates could be observed and were distributed randomly about the trough surface. The second drop then spread, and apart from depositing more material, pushed the floating MoS₂ deposited in the first drop towards the trough edge. As more and more material was added, more of the islands were pushed towards the edge of the trough by the spreading front of the solvent and, as shown in Fig. 3b, a faint continuous film could be observed. As is apparent from the videos, when the solvent spreading front reached the film, the evaporation and contraction of the spreading solvent lead to the rearrangement of the MoS₂ with each additional drop. However, several centimeters into the film, the material appears to have formed a nearly incompressible solid phase. As the film grows further, a clear circular boundary was made by the spreading drop as it compressed more material against the film. When the circular boundary was only a few centimeters in diameter, the solvent could not evaporate before the next drop was added which resulted in the pooling of the dispersion and formation of a liquid lens at the center of the trough. This 2D aggregation behaviour of MoS₂ nanosheets at air-water interface is also affected by the MoS₂ concentration. Specifically, when the initial MoS₂ concentration is high (~ 0.2 mg mL⁻¹), the MoS₂ tend to form islands early in the spreading process. When the initial MoS₂ concentration is low (~ 0.05 mg mL⁻¹), the solid phase of the film is not observed until the later stages of spreading. This suggests that the MoS₂ nanosheets can act as repulsive, floating particles under certain deposition conditions. A more detailed study regarding the effects of MoS₂ concentration on the aggregation behaviour and the final film formation will be carried out in the future.

From these videos, we hypothesize that the lateral pressure from the spreading solvent plays an important role in the film densification. When a solvent is spread at the air-water interface, the change in interfacial tensions between the air-water interface and the newly formed liquid-liquid and liquid-air interfaces dominates the spreading process once the film is thin enough that gravity no longer plays a role.⁴⁸ At the leading edge of the spreading front, the gradient of the interfacial tension (*i.e.* the Marangoni effect) at the boundary also contributes to the force which acts on the growing film.⁴⁹ These forces are likely responsible for the film densification in our repetitive dripping process. The thermodynamic spreading pressure (S) could be estimated for the system if the solvent-air (γ_{sa}), water-air (γ_{wa}) and solvent-water (γ_{sw}) interfacial tensions were known according to $S = \gamma_{wa} - \gamma_{sa} - \gamma_{sw}$. For pure DCE these values are known,

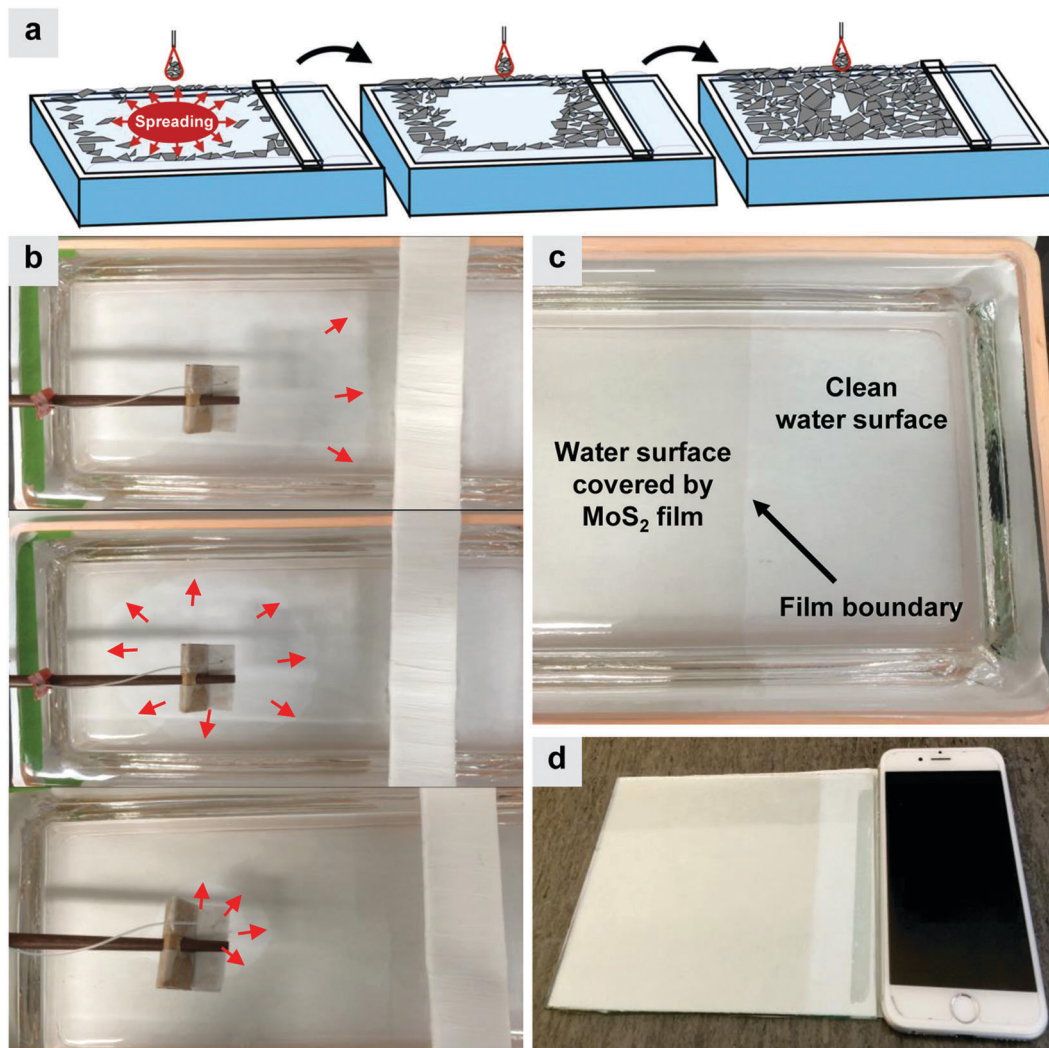


Fig. 3 (a) Schematic illustration of the spreading-assisted assembly process. (b) Video snapshots of film growth as a function of time. Due to the transparency of the growing film, red arrows are used to guide the reader's eye. The film grows from the trough edge towards the center. The white bar is the fixed barrier (c) photograph of a stable MoS₂ thin film floating on the water surface after the fixed barrier is removed. (d) Photograph of a large-area coating of MoS₂ film on a glass substrate deposited by the horizontal precipitation method (*i.e.* lowering the film onto the glass by withdrawing sub-phase water from the coating bath). A smartphone is used for scale.

and thus S for pure DCE is estimated to be $S_{\text{DCE}} = 72.5 - 32.23 - 28.2 = 12.1 \text{ mN m}^{-1}$.^{50,51} Due to the miscibility of DMF with water, $\gamma_{\text{DMF-water}}$ cannot be easily determined experimentally but is expected to be smaller than $\gamma_{\text{DCE-water}}$ due to the more favorable polar-polar interactions between the two liquids while $\gamma_{\text{DMF-air}}$ is slightly larger at 37.1 mN m^{-1} . Thus, the spreading coefficient for DMF is expected to be similar to that of DCE. Comparing these values to the pressure exerted by the moveable barriers to compress the film above, as well as the typical pressures required to achieve solidification of lipids and similar 2D nanomaterials like graphene oxide, it seems plausible that the solvent spreading pressure exerted by the solvent on the film during material deposition is capable of condensing the floating material into a solid phase. Cote *et al.* reported that graphene oxide single sheets were able to sustain surface pressures up to 30 mN m^{-1} at the air-water interface before the sheets started folding and overlapping at the sheet edges³⁶ and from our estimates above,

the spreading pressure exerted by the solvent should be well below this. By using this barrier-free spreading-assisted assembly approach, we are able to deposit a film as large as the trough area. As shown in Fig. 3d, a uniform film $\sim 130 \text{ cm}^2$ in area can be coated, which is about twice the size of a large screen size smartphone. The upper limit of the film area produced by our assembly method may be further increased by using a larger trough. A similar phenomenon has been reported for other materials. For example, Kim *et al.* reported the self-assembly of multi-walled carbon nanotubes, Ketjen-Black carbon, super-P carbon and silica nanospheres by continuous injection of the suspension at the air-water interface.⁵² This method allowed them to obtain a densely packed film with only the assistance of solvent spreading. However, they were unable to achieve monolayer film thickness. On the other hand, Zhang *et al.* reported the self-assembly of LB films of graphene-based molybdenum oxide nanohybrid sheets (mRGO-MoO_{3-x}) by repetitively dripping *via* a similar method to

ours and were able to produce molecular monolayers but could not control film density as their demonstration was carried out in a small beaker.⁵³

We further investigated the effects of MoS₂ concentration on the properties of the final film. We prepared three dispersions with different MoS₂ concentration (*i.e.* 0.22 mg mL⁻¹, 0.11 mg mL⁻¹, 0.055 mg mL⁻¹) and repeated the spreading experiment. By knowing the mass of material deposited and the trough area, a transfer efficiency can be estimate in terms of what we will refer to as the Langmuir specific surface area (LSSA) calculated using the following formula:

$$\text{LSSA}(\text{m}^2 \text{g}^{-1}) = \frac{A_{\text{film}}}{\nu \times t \times C}, \quad (1)$$

where A_{film} is the total area of the film on water surface, ν is the deposition rate (in mL min⁻¹) controlled by the syringe pump, t is the total deposition time and C is the MoS₂ concentration. Fig. 4 shows that the average LSSA increases as the dispersion is diluted. This may be due to the fact that the probability of the overlapping of MoS₂ nanosheets during the spreading process decreases as the MoS₂ concentration decreases. However, the difference in LSSA is relatively small, at least for the 0.011 and 0.055 mg mL⁻¹ cases. This indicates that the overlapping is not significant as we increase the MoS₂ concentration. Therefore, the thickness of the final film may only depend on the thickness of the initial MoS₂ nanosheets.

Assuming that the film deposited is fully dense (which will be discussed later) it is possible to estimate the expected LSSA for a single layer of MoS₂ from crystal lattice parameters. Given the unit cell for 2H MoS₂ has lattice vectors $\bar{a} = (a, 0, 0)$, $\bar{b} = \left(\frac{a}{2}, \frac{\sqrt{3}a}{2}, 0\right)$, $\bar{c} = (0, 0, c)$, where $a = 3.125 \text{ \AA}$,⁵⁴ we can calculate the area of the top-facing side of the unit cell as 8.457 Å². The mass of a MoS₂ single layer per unit cell, m , is 160.07 g mol⁻¹. Thus, the LSSA is given by:

$$\text{LSSA} = \frac{A \times N_a}{m} = 318 \text{ m}^2 \text{g}^{-1} \quad (2)$$

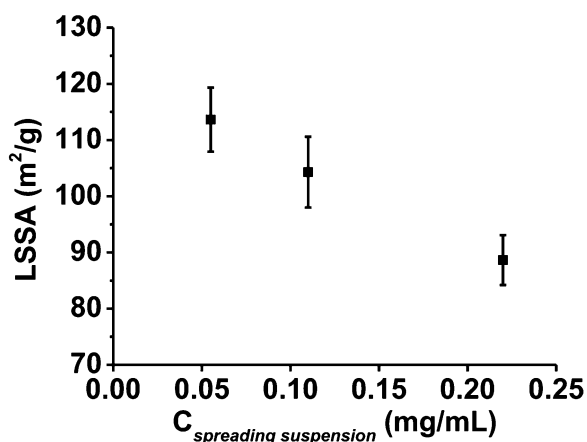


Fig. 4 The effect of the MoS₂ spreading suspension concentration on the Langmuir specific surface area (*i.e.* LSSA).

Alternatively, the LSSA can be roughly calculated by multiplying the bulk MoS₂ density by the monolayer spacing and inverting the result, giving an LSSA of 321 m² g⁻¹, which is in very good agreement with the previous calculation. To compare this to the widely reported specific surface area of graphene (2630 m² g⁻¹), we multiply our LSSA by a factor of two to account for the surface area on both sides of the sheet which leads to the theoretical specific surface area of MoS₂ being about 636 m² g⁻¹. Interestingly, despite the large volume of work done on MoS₂, to our knowledge, this number has not been reported previously. Knowing the theoretical value of the LSSA allows us to estimate an average layer thickness for our film deposited from 0.055 mg mL⁻¹ of $\sim 318/112 = 2.8$ layers assuming the film is fully dense.

To determine the film coverage and sheet thicknesses, we took AFM images of the films deposited from various areas in the trough. Fig. 5a shows a relatively large magnification ($\sim 10 \times 10 \mu\text{m}$) AFM image of our MoS₂ deposited onto a mica substrate at a concentration of 0.055 mg mL⁻¹, wherein a high density of tiled MoS₂ sheets is observed. Zooming into the third quadrant of this image (Fig. 5b), the exposed mica substrate can be seen more easily. Manually extracting the height profiles at substrate–monolayer and monolayer–bilayer junctions, as shown in Fig. 5c, indicates an average MoS₂ layer thickness of ~ 1.34 nm. Interestingly, the average substrate–monolayer thickness is significantly larger at 1.97 nm, likely due to surface defects or leftover spreading solvent trapped under the monolayers. These values are in line with previously reported thicknesses of chemically-exfoliated MoS₂ deposited onto silicon substrates.⁵⁵ As mentioned in the Experimental Methods section, the sheet thickness distribution of our film was determined by fitting the sum of Gaussian line-shapes to the height profile data. This is shown for the third quadrant in Fig. 5d, with the inset showing the output of this analysis. The first Gaussian fit around 2 nm corresponds to the substrate and gives an indication of the uncertainty in this estimate (standard deviation ~ 0.4 nm) due to difficulties in leveling the entire image. Repeating this operation on all 4 quadrants of our film, the estimate indicates that, for this sample, we achieve 83% surface coverage, with 35% of the surface being covered by monolayers, 12% covered by bilayers, and the remaining 36% of the surface being covered by trilayers or larger. This was one of the lowest coverage samples observed and is displayed to make the contrast between sheets and substrate more apparent to the reader. The coverage estimated in all AFM images analyzed suggests that the films are most often between 85 and 95% density. Overall, we find average sheet thicknesses of 2.7, 2.6, and 2.8 layers for the 0.055, 0.11, and 0.22 mg mL⁻¹ depositions, respectively. This corresponds to LSSAs of 120, 124, and 113 m² g⁻¹, from low to high concentrations, implying that the LSSA is not a function of concentration. This is in contrast to the results shown in Fig. 4 which demonstrated that the LSSA decreases slightly with increasing concentration. This discrepancy may be a result of the fact that the experimentally determined LSSA takes sub-phase loss into account, whereas the AFM determined LSSA does not. This might imply that higher concentration dispersions result in

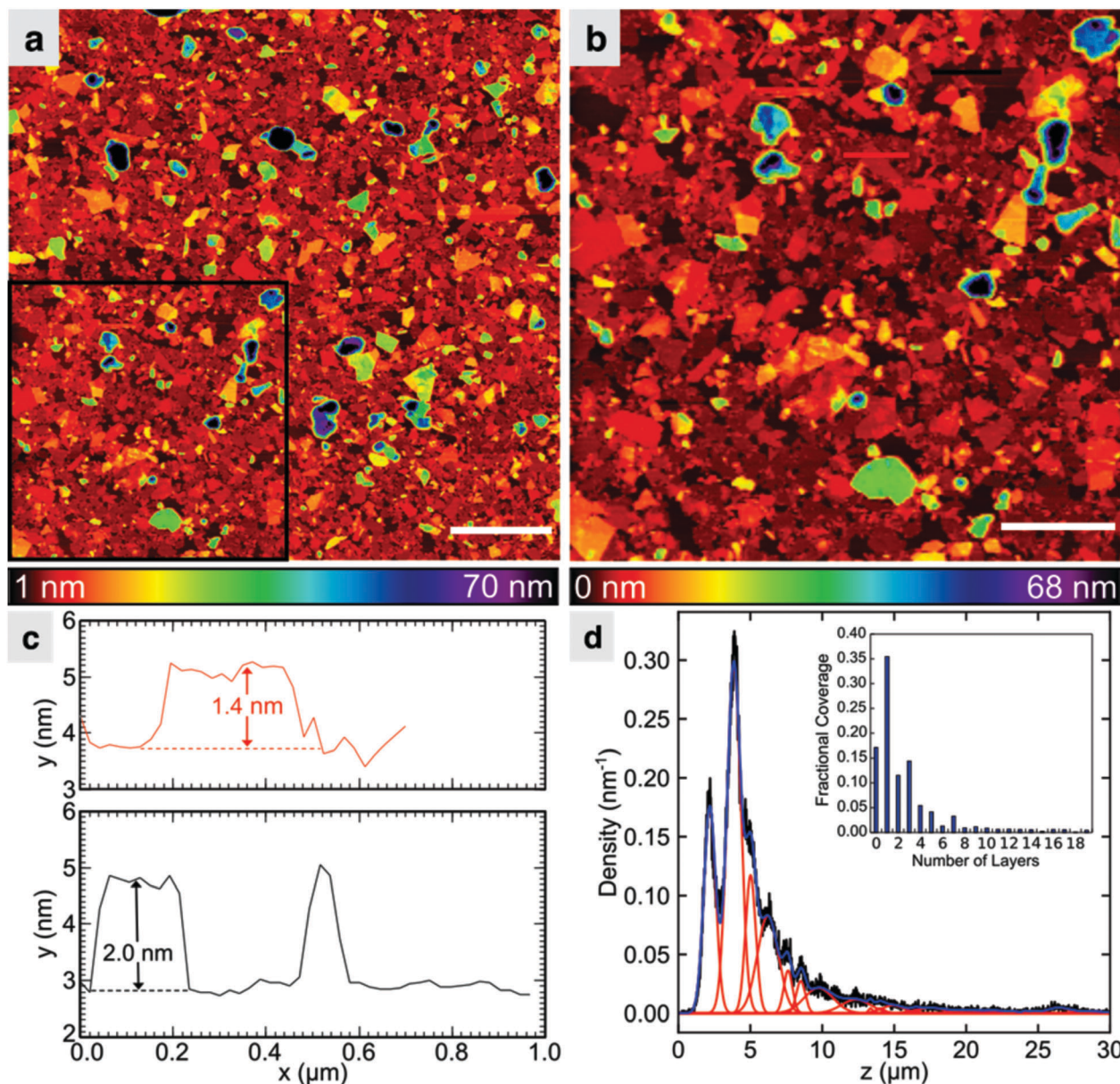


Fig. 5 (a) AFM image of the as-prepared MoS₂ film on a mica substrate deposited from a 0.055 mg mL⁻¹ dispersion. The scale bar is 2 μm. (b) Magnified view of region indicated in (a). The scale bar is 1 μm. (c) Height profiles of monolayer–bilayer and substrate–monolayer junctions extracted from the red and black lines in (b), respectively. (d) Height distribution of image shown in (b) with Gaussian fits shown. The inset shows the fractional coverage estimated by the area under each Gaussian for each layer number with layer '0' being the substrate.

greater sub-phase loss, with the 0.055 mg mL⁻¹ dispersion undergoing almost no sub-phase loss at all. However, due to the small variations in our LSSA (calculated by either method) and the uncertainty in our analysis, a more rigorous statistical study on many more films would have to be carried out. Therefore, our assumption of a fully dense film in the LSSA analysis is an underestimate by about 10%.

Optical and electrical properties of films

Using this spreading-assisted assembly method, we repeatedly coated glass substrates (Fig. 6a inset) and measured their transmittance. As shown in Fig. 6a, the transmittance of a single-coating

film at 550 nm is around 90%. This value is comparable to that reported for a 2H phase MoS₂ thin film prepared by the CVD method.⁵⁶ The transmittance decreased by about 8–10% per layer deposited. Raman spectroscopy results are shown in Fig. 6b. 2H MoS₂ has two main Raman modes: the in-plane mode, E_{2g}¹, and the out-of-plane mode, A_{1g}. After chemical exfoliation, we observed three distinguished features in the case of 1T MoS₂ labeled as J₁, J₂ and J₃ peaks at 154.0 cm⁻¹, 226.1 cm⁻¹ and 326.4 cm⁻¹. These peak intensities, characteristic of the 1T polymorph, decreased after being annealed at 150 °C, suggesting restoration of the 2H polymorph and confirming previous reports.^{4,9} Furthermore, the A_{1g} mode shifted from 408.2 cm⁻¹

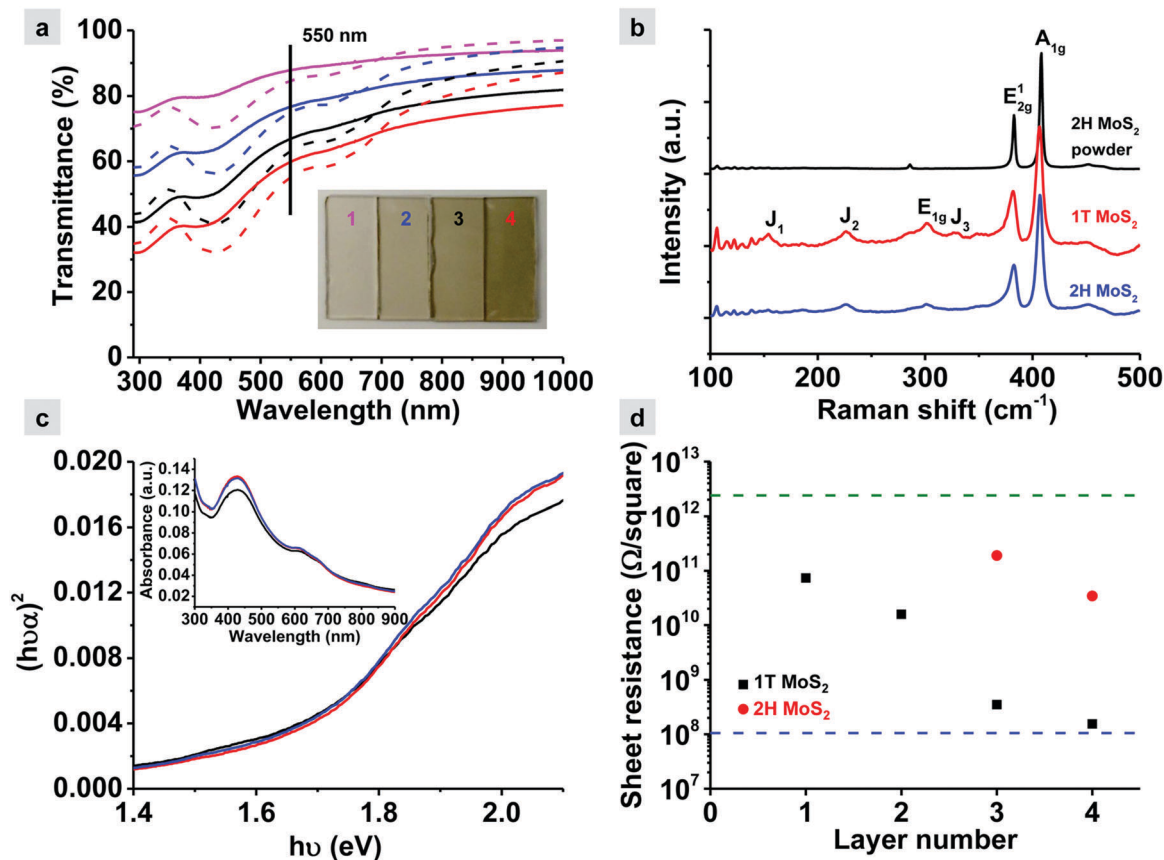


Fig. 6 (a) Transmittance study of the as-made MoS₂ films (solid line: 1T, dash line: 2H) as a function of different coating layers. Magenta: one-layer coating; blue: two-layer coatings; black: three-layer coatings; red: four-layer coatings. The inset shows the as-prepared 1T MoS₂ thin film coated glass slides. (b) Raman spectra of bulk MoS₂ powder (black), as-prepared 1T MoS₂ thin film (red), as-prepared 2H MoS₂ thin film (blue). The spectra are normalized to the intensity of A_{1g} peak. (c) Tauc plot of as-prepared 2H MoS₂ thin film. Three curves represent three samples from the same batch. The inset shows the optical depth corresponding to a single coating. (d) Sheet resistance measurements of as-prepared 1T (black) and 2H (red) MoS₂ thin film as a function of different coating layers. The green and blue line represent upper and lower measurement limits.

to 406.7 cm⁻¹ for bulk and monolayer samples, respectively, while the E_{2g}¹ mode remained consistent at 382.7 cm⁻¹. This is also evidence that suggests that the films formed are only a few-layers in thickness.⁴

The inset of Fig. 6c shows optical absorbance measurements of as-prepared MoS₂ films after heat treatment was carried out on a one-layer deposition. Much more pronounced A and B excitonic transitions were observed at ~660 and ~610 nm in all samples, suggesting restoration of the 2H polymorph after heat treatment.⁴ In order to estimate the number of layers in the film from optical absorbance results, we approximate the film as being uniform in thickness. The estimated average layer number can be correlated to the optical depth *A*, (in OD), which is given by

$$A = \alpha \cdot s \ln(10) \quad (3)$$

where *s* is the thin film thickness, α is absorption coefficient which is given by $\alpha = 4\pi k/\lambda = 4\pi k f/c$. Therefore, eqn (2) can be rewritten as:

$$A = 4\pi k \cdot N \cdot t \ln(10)/\lambda \quad (4)$$

where *t* is the thickness per layer (assumed to be 0.7 nm), *N* is the number of layers, and λ is the wavelength. Yim *et al.*⁵⁷ reported that *k* for MoS₂ is approximately 1 for illumination with a 600 nm wavelength and we measured 0.06 for the OD at the same wavelength. Therefore, we are able to estimate that the film is approximately 2.5 layers thick, which is in line with the value we obtained from both our LSSA estimate (2.9 layers) as well as the AFM analysis (2.7 layers).

We also investigated the photoluminescence properties of our samples. However, our films gave very weak photoluminescence responses using a standard spectrometer. Therefore, instead, we further analyzed the absorbance data using a Tauc analysis to determine the average optical gap in the film.^{57–59} Fig. 6c shows a direct band gap Tauc analysis carried out on the absorbance data collected from three different MoS₂ LB films (one deposition thick). The results suggested an absorption tail to about 1.6 eV followed by a regime from 1.7 to 2.0 eV that could readily be fit with a linear function. The extrapolation of that fitted function consistently predicted direct bandgaps of about 1.6 eV for the various samples tested. A similar analysis was carried out using an indirect bandgap Tauc analysis and a linear fit seemed appropriate in the range of 2.2–2.7 eV,

which suggested bandgaps of about 1.2 eV. However, such a value seems inappropriate compared to literature values.^{57,60} This suggests that the direct bandgap analysis is more appropriate for the films studied here. Given our discussion above, all data suggests that our film has an average layer number between 2 and 3 with a large percentage of monolayers (~45%) and bilayers (13%). One would generally expect monolayer MoS₂ to be a direct semiconducting material, while the multi-layer (bilayer and thicker) are generally considered to be indirect semiconducting materials. However, recent works have shown that bilayer films may still have a direct bandgap due to superlattice,⁶¹ orientation,⁶² and lattice spacing⁶³ effects.

The resistances of our as-prepared MoS₂ films were measured using a soft contacting technique. A laser patterned ITO/carbon tape electrode structure was simply pressed against the film, avoiding the need for cleanroom deposition. This resulted in a 100 μm gap between the two electrodes over a length of 408 mm. Fig. 6d shows the layer-dependent sheet resistivity measurement before and after heat treatment of the MoS₂ films. A decrease in sheet resistance of approximately an order of magnitude per layer was observed. This indicates that our deposition method provides high control over layer numbers as well as film uniformity and reproducibility. We also observed that the heat-treated films are approximately 3 orders of magnitude less conductive than the films which have a larger proportion of 1T. This is consistent with the expectation of the enrichment of the 2H polymorph upon heating. We note that 1 and 2 layer semiconducting films were tested. However, their resistances were above the upper sensitivity limit of the fixture used. When compared with previous reports, our films appear to have a much lower conductivity. However, this can be explained by the much larger gap width (100 μm) compared to other works and a potentially different ratio of 1T/2H polymorphs in the deposited films prior to annealing.^{4,5} Resistance through the MoS₂ is comprised of two main factors: in-sheet resistance (intrinsic) and sheet-to-sheet or percolation resistance. While the intrinsic resistance is independent of electrode separation, the much higher percolation resistance is not. Wider electrode separation means electrons must hop from nanosheet to nanosheet more times to reach an electrode. For example, Eda *et al.* reported the resistivity of films deposited by vacuum filtration to be ~1 MΩ sq⁻¹ but used contacts which were 20–50 μm apart.^{4,5} Our four-layer films with larger contact separation are measured to be about 100 MΩ sq⁻¹. While the long range conductivities of the Langmuir films deposited by this approach are low, it is likely that this material would be interfaced with other transparent conductors such as graphene or ITO in a device architecture. Due to the high resistance between the flakes, such a device would not rely on charge transfer laterally through the film but within the nanometer-scale thickness of the deposited layers. The method presented provides a convenient way to carry out this coupling over large areas and may be useful to engineer a wide variety of heterostructure-based optoelectronic devices such as thin film solar cells or large area, transparent electrodes for photoelectrochemical water splitting.

Conclusions

We have demonstrated a mixed-solvent, colloidal dispersion which enables the high yield deposition (up to 120 m² g⁻¹) of chemically exfoliated MoS₂ nanosheets onto the air–water interface. Upon deposition, we observed a 2D aggregation phenomenon during traditional Langmuir–Blodgett deposition, despite the large negative zeta potential of the sheets in water. Taking advantage of this phenomenon, we studied the solvent spreading-assisted assembly and deposition of large area, transparent, densely-packed MoS₂ films which could be prepared without barrier compression. Video analysis of film formation suggests that forces induced by solvent spreading (including the Marangoni effect) are responsible for the film densification. The high density and uniformity of these films allow us to directly assess exfoliation efficiency and to estimate film thickness or exfoliation efficiency by comparing the transfer efficiency to the theoretical specific surface area of MoS₂, estimated to be 636 m² g⁻¹ (the area of two sides of the MoS₂ nanosheet). Furthermore, the directionality of the 2D aggregation process lends itself to be adapted to continuous film transfer methods which will provide a simple and versatile path towards well-controlled coatings for advanced electronic and optoelectronic applications.

Acknowledgements

The authors would like to acknowledge funding support from the National Science and Engineering Council of Canada's Discovery Grant program.

Notes and references

- 1 B. Radisavljevic, A. Radenovic, J. Brivio, V. Giacometti and A. Kis, Single-layer MoS₂ transistors, *Nat. Nanotechnol.*, 2011, **6**(3), 147–150.
- 2 K. F. Mak, C. Lee, J. Hone, J. Shan and T. F. Heinz, Atomically Thin MoS₂: A New Direct-Gap Semiconductor, *Phys. Rev. Lett.*, 2010, **105**(13), 136805.
- 3 B. Han and Y. H. Hu, MoS₂ as a co-catalyst for photocatalytic hydrogen production from water, *Energy Sci. Eng.*, 2016, **4**(5), 285–304.
- 4 G. Eda, H. Yamaguchi, D. Voiry, T. Fujita, M. Chen and M. Chhowalla, Photoluminescence from Chemically Exfoliated MoS₂, *Nano Lett.*, 2011, **11**(12), 5111–5116.
- 5 M. Acerce, D. Voiry and M. Chhowalla, Metallic 1T phase MoS₂ nanosheets as supercapacitor electrode materials, *Nat. Nanotechnol.*, 2015, **10**(4), 313–318.
- 6 M.-L. Tsai, S.-H. Su, J.-K. Chang, D.-S. Tsai, C.-H. Chen and C. Wu, *et al.*, Monolayer MoS₂ Heterojunction Solar Cells, *ACS Nano*, 2014, **8**(8), 8317–8322.
- 7 C. B. Roxlo, R. R. Chianelli, H. W. Deckman, A. F. Ruppert and P. P. Wong, Bulk and surface optical absorption in molybdenum disulfide, *J. Vac. Sci. Technol., A*, 1987, **5**(4), 555–557.
- 8 X. R. Qin, D. Yang, R. F. Frindt and J. C. Irwin, Real-space imaging of single-layer MoS₂ by scanning tunneling

- microscopy, *Phys. Rev. B: Condens. Matter Mater. Phys.*, 1991, **44**(7), 3490–3493.
- 9 K. C. Knirsch, N. C. Berner, H. C. Nerl, C. S. Cucinotta, Z. Gholamvand and N. McEvoy, *et al.*, Basal-Plane Functionalization of Chemically Exfoliated Molybdenum Disulfide by Diazonium Salts, *ACS Nano*, 2015, **9**(6), 6018–6030.
 - 10 S. B. Desai, S. R. Madhvapathy, A. B. Sachid, J. P. Llinas, Q. Wang and G. H. Ahn, *et al.*, MoS₂ transistors with 1-nanometer gate lengths, *Science*, 2016, **354**(6308), 99–102.
 - 11 Z. Yin, H. H. Li, H. H. Li, L. Jiang, Y. Shi and Y. Sun, *et al.*, Single-layer MoS₂ phototransistors, *ACS Nano*, 2012, **6**(1), 74–80.
 - 12 M. Bernardi, M. Palummo and J. C. Grossman, Extraordinary sunlight absorption and one nanometer thick photovoltaics using two-dimensional monolayer materials, *Nano Lett.*, 2013, **13**(8), 3664–3670.
 - 13 E. G. da Silveira Firmiano, A. C. Rabelo, C. J. Dalmaschio, A. N. Pinheiro, E. C. Pereira and W. H. Schreiner, *et al.*, Supercapacitor Electrodes Obtained by Directly Bonding 2D MoS₂ on Reduced Graphene Oxide, *Adv. Energy Mater.*, 2014, **4**(6), 1301380.
 - 14 A. Winchester, S. Ghosh, S. Feng, A. L. Elias, T. Mallouk and M. Terrones, *et al.*, Electrochemical Characterization of Liquid Phase Exfoliated Two-Dimensional Layers of Molybdenum Disulfide, *ACS Appl. Mater. Interfaces*, 2014, **6**(3), 2125–2130.
 - 15 R. Samnakay, C. Jiang, S. L. Romyantsev, M. S. Shur and A. A. Balandin, Selective chemical vapor sensing with few-layer MoS₂ thin-film transistors: comparison with graphene devices, *Appl. Phys. Lett.*, 2015, **106**(2), 023115.
 - 16 B. Hinnemann, P. G. Moses, J. Bonde, K. P. Jørgensen, J. H. Nielsen and S. Horch, *et al.*, Biomimetic Hydrogen Evolution: MoS₂ Nanoparticles as Catalyst for Hydrogen Evolution, *J. Am. Chem. Soc.*, 2005, **127**(15), 5308–5309.
 - 17 M. Calandra, Chemically exfoliated single-layer MoS₂: stability, lattice dynamics, and catalytic adsorption from first principles, *Phys. Rev. B: Condens. Matter Mater. Phys.*, 2013, **88**(24), 245428.
 - 18 Y. Yin, J. Han, Y. Zhang, X. Zhang, P. Xu and Q. Yuan, *et al.*, Contributions of Phase, Sulfur Vacancies, and Edges to the Hydrogen Evolution Reaction Catalytic Activity of Porous Molybdenum Disulfide Nanosheets, *J. Am. Chem. Soc.*, 2016, **138**(25), 7965–7972.
 - 19 M. A. Lukowski, A. S. Daniel, F. Meng, A. Forticaux, L. Li and S. Jin, Enhanced Hydrogen Evolution Catalysis from Chemically Exfoliated Metallic MoS₂ Nanosheets, *J. Am. Chem. Soc.*, 2013, **135**(28), 10274–10277.
 - 20 Q. Ding, B. Song, P. Xu and S. Jin, Efficient Electrocatalytic and Photoelectrochemical Hydrogen Generation Using MoS₂ and Related Compounds, *Chem.*, 2016, **1**(5), 699–726.
 - 21 Y. Liu, Y.-X. Yu and W. Zhang, MoS₂/CdS Heterojunction with High Photoelectrochemical Activity for H₂ Evolution under Visible Light: The Role of MoS₂, *J. Phys. Chem. C*, 2013, **117**(25), 12949–12957.
 - 22 M. Chhowalla, H. S. Shin, G. Eda, L. Li, K. P. Loh and H. Zhang, The chemistry of two-dimensional layered transition metal dichalcogenide nanosheets, *Nat. Chem.*, 2013, **5**(4), 263–275.
 - 23 P. Joensen, R. F. Frindt and S. R. Morrison, Single-Layer MoS₂, *Mater. Res. Bull.*, 1986, **21**(4), 457–461.
 - 24 C. Muratore, J. J. Hu, B. Wang, M. A. Haque, J. E. Bultman and M. L. Jespersen, *et al.*, Continuous ultra-thin MoS₂ films grown by low-temperature physical vapor deposition, *Appl. Phys. Lett.*, 2014, **104**(26), 261604.
 - 25 X. Yu, M. S. Prévot, N. Guijarro and K. Sivula, Self-assembled 2D WSe₂ thin films for photoelectrochemical hydrogen production, *Nat. Commun.*, 2015, **6**(May), 7596.
 - 26 W. M. R. Divigalpitiya, S. R. Morrison and R. F. Frindt, Thin oriented films of molybdenum disulphide, *Thin Solid Films*, 1990, **186**(1), 177–192.
 - 27 G. L. Gaines, *Insoluble Monolayer at Liquid-Gas Interfaces*, Interscience Publishers, New York, 1966.
 - 28 C. P. Collier, Reversible Tuning of Silver Quantum Dot Monolayers Through the Metal-Insulator Transition, *Science*, 1997, **277**(5334), 1978–1981.
 - 29 P. Yang and F. Kim, Langmuir–Blodgett assembly of one-dimensional nanostructures, *ChemPhysChem*, 2002, **3**(6), 503–506.
 - 30 J.-H. Lee, W.-S. Kang, C. K. Najeeb, B.-S. Choi, S.-W. Choi and H. J. Lee, *et al.*, A hydrogen gas sensor using single-walled carbon nanotube Langmuir–Blodgett films decorated with palladium nanoparticles, *Sens. Actuators, B*, 2013, **188**, 169–175.
 - 31 S. W. Choi, W. S. Kang, J. H. Lee, C. K. Najeeb, H. S. Chun and J. H. Kim, Patterning of hierarchically aligned single-walled carbon nanotube langmuir-blodgett films by micro-contact printing, *Langmuir*, 2010, **26**(19), 15680–15685.
 - 32 X. Li, L. Zhang, X. Wang, I. Shimoyama, X. Sun and W. K. Seo, *et al.*, Langmuir–Blodgett assembly of densely aligned single-walled carbon nanotubes from bulk materials, *J. Am. Chem. Soc.*, 2007, **129**(16), 4890–4891.
 - 33 J. Kim, L. J. Cote, F. Kim, W. Yuan, K. Shull and J. Huang, Graphene Oxide Sheets at Interfaces, *J. Am. Chem. Soc.*, 2010, **132**(14), 8180–8186.
 - 34 H. L. Nie, X. Dou, Z. Tang, H. D. Jang and J. Huang, High-Yield Spreading of Water-Miscible Solvents on Water for Langmuir–Blodgett Assembly, *J. Am. Chem. Soc.*, 2015, **137**(33), 10683–10688.
 - 35 Q. Zheng, L. Shi and J. Yang, Langmuir–Blodgett assembly of ultra-large graphene oxide films for transparent electrodes, *Trans. Nonferrous Met. Soc. China*, 2012, **22**(10), 2504–2511.
 - 36 L. J. Cote, F. Kim and J. Huang, Langmuir–Blodgett Assembly of Graphite Oxide Single Layers, *J. Am. Chem. Soc.*, 2009, **131**(3), 1043–1049.
 - 37 J. D. Mangadla, C. M. Santos and M. J. L. Felipe, de Leon a CC, Rodrigues DF, Advincula RC. On the antibacterial mechanism of graphene oxide (GO) Langmuir–Blodgett films, *Chem. Commun.*, 2015, **51**(14), 2886–2889.
 - 38 X. Li, G. Zhang, X. Bai, X. Sun, X. Wang and E. Wang, *et al.*, Highly conducting graphene sheets and Langmuir–Blodgett films, *Nat. Nanotechnol.*, 2008, **3**(9), 538–542.

- 39 Y. Taguchi, R. Kimura, R. Azumi, H. Tachibana, N. Koshizaki and M. Shimomura, *et al.*, Fabrication of Hybrid Layered Films of MoS₂ and an Amphiphilic Ammonium Cation Using the Langmuir–Blodgett Technique, *Langmuir*, 1998, **14**(22), 6550–6555.
- 40 M. A. Pope, C. Punckt and I. A. Aksay, Intrinsic Capacitance and Redox Activity of Functionalized Graphene Sheets, *J. Phys. Chem. C*, 2011, **115**(41), 20326–20334.
- 41 H.-J. Butt, K. Graf and M. Kappl, *Physics and Chemistry of Interfaces*, John Wiley, FRG: Wiley-VCH Verlag GmbH & Co. KgaA, Weinheim, 2003.
- 42 G. Eda, T. Fujita, H. Yamaguchi, D. Voiry, M. Chen and M. Chhowalla, Coherent atomic and electronic heterostructures of single-layer MoS₂, *ACS Nano*, 2012, **6**(8), 7311–7317.
- 43 A. Goloveshkin, Structural Properties and Phase Transition of Exfoliated-Restacked Molybdenum Disulfide, *J. Phys. Chem. C*, 2013, **117**(16), 8509–8515.
- 44 G. Ma, H. Peng, J. Mu, H. Huang, X. Zhou and Z. Lei, In situ intercalative polymerization of pyrrole in graphene analogue of MoS₂ as advanced electrode material in supercapacitor, *J. Power Sources*, 2013, **229**, 72–78.
- 45 W. Liu, X. Yang, Y. Zhang, M. Xu and H. Chen, Ultra-stable two-dimensional MoS₂ solution for highly efficient organic solar cells, *RSC Adv.*, 2014, **4**(62), 32744–32748.
- 46 P. Joensen, R. F. Frindt and S. R. Morrison, Single-layer MoS₂, *Mater. Res. Bull.*, 1986, **21**(4), 457–461.
- 47 G. J. Silverberg, P. Pearce and C. D. Vecitis, Controlling self-assembly of reduced graphene oxide at the air-water interface: Quantitative evidence for long-range attractive and many-body interactions, *ACS Appl. Mater. Interfaces*, 2015, **7**(6), 3807–3815.
- 48 C. Huh, M. Inoue and S. Mason, Uni-directional spreading of one liquid on the surface of another, *Can. J. Chem. Eng.*, 1975, **53**, 367–371.
- 49 A. D. Dussaud and S. M. Troian, Dynamics of spontaneous spreading with evaporation on a deep fluid layer, *Phys. Fluids*, 1998, **10**(1), 23–38.
- 50 B. Hou, N. Laanait, H. Yu, W. Bu, J. Yoon and B. Lin, *et al.*, Ion distributions at the water/1,2-dichloroethane interface: Potential of mean force approach to analyzing X-ray reflectivity and interfacial tension measurements, *J. Phys. Chem. B*, 2013, **117**(17), 5365–5378.
- 51 J. A. Dean, *Lange's Handbook of Chemistry*, McGraw-Hill, Inc., New York, 1999, p. 5.93.
- 52 M. S. Kim, L. Ma, S. Choudhury, S. S. Moganty, S. Wei and L. A. Archer, Fabricating multifunctional nanoparticle membranes by a fast layer-by-layer Langmuir? Blodgett process: application in lithium? sulfur batteries, *J. Mater. Chem. A*, 2016, **4**(38), 14709–14719.
- 53 H. Zhang, K.-W. Jeon and D.-K. Seo, Equipment-Free Deposition of Graphene-Based Molybdenum Oxide Nano-hybrid Langmuir–Blodgett Films for Flexible Electrochromic Panel Application, *ACS Appl. Mater. Interfaces*, 2016, **8**(33), 21539–21544.
- 54 A. Molina-Sánchez and L. Wirtz, Phonons in single-layer and few-layer MoS₂ and WS₂, *Phys. Rev. B: Condens. Matter Mater. Phys.*, 2011, **84**(15), 155413.
- 55 X. Fan, P. Xu, Y. C. Li, D. Zhou, Y. Sun and M. A. T. Nguyen, *et al.*, Controlled Exfoliation of MoS₂ Crystals into Trilayer Nanosheets, *J. Am. Chem. Soc.*, 2016, **138**(15), 5143–5149.
- 56 Y. Lee, J. Lee, H. Bark, I.-K. Oh, G. H. Ryu and Z. Lee, *et al.*, Synthesis of wafer-scale uniform molybdenum disulfide films with control over the layer number using a gas phase sulfur precursor, *Nanoscale*, 2014, **6**(5), 2821–2826.
- 57 C. Yim, M. O'Brien, N. McEvoy, S. Winters, I. Mirza and J. G. Lunney, *et al.*, Investigation of the optical properties of MoS₂ thin films using spectroscopic ellipsometry, *Appl. Phys. Lett.*, 2014, **104**(10), 103114.
- 58 J. T. Tauc and R. Grigorovici, Optical Properties and Electronic Structure of Amorphous Germanium, *Phys. Status Solidi B*, 1966, **15**, 627.
- 59 G. Papadimitropoulos, N. Vourdas, A. Kontos, M. Vasilopoulou, D. N. Kouvatso and N. Boukos, *et al.*, Hot-wire vapor deposition of amorphous MoS₂ thin films, *Phys. Status Solidi C*, 2015, **12**(7), 969–974.
- 60 J. W. Park, H. S. So, S. Kim, S.-H. Choi, H. Lee and J. Lee, *et al.*, Optical properties of large-area ultrathin MoS₂ films: Evolution from a single layer to multilayers, *J. Appl. Phys.*, 2014, **116**(18), 183509.
- 61 J. T. Jiang, S. L. Xiu, M. M. Zheng, T. T. Jia, H. Y. Liu and Y. Zhang, *et al.*, Indirect–direct bandgap transition and gap width tuning in bilayer MoS₂ superlattices, *Chem. Phys. Lett.*, 2014, **613**, 74–79.
- 62 Z. Wang, Q. Chen and J. Wang, Electronic Structure of Twisted Bilayers of Graphene/MoS₂ and MoS₂/MoS₂, *J. Phys. Chem. C*, 2015, **119**(9), 4752–4758.
- 63 J. Xiao, M. Long, X. Li, Q. Zhang, H. Xu and K. S. Chan, Effects of van der Waals interaction and electric field on the electronic structure of bilayer MoS₂, *J. Phys.: Condens. Matter*, 2014, **26**(40), 405302.